Please provide feedback

Please support the ScholarWorks@UMBC repository by emailing scholarworks-group@umbc.edu and telling us what having access to this work means to you and why it's important to you. Thank you.

Malic Acid Carbon Dots: From Super-resolution Live-Cell Imaging to Highly Efficient Separation

Bo Zhi,[†,¶] Yi Cui,[‡,¶] Shengyang Wang,[†] Benjamin P. Frank,[§] Denise N. Williams,[⊥] Richard P. Brown,[⊥] Eric S. Melby,[‡,#] Robert J. Hamers,[∥] Zeev Rosenzweig,[⊥] D. Howard Fairbrother,[§] Galya Orr,*[‡] and Christy L. Haynes*[†]

†Department of Chemistry, University of Minnesota—Twin Cities, Minneapolis, Minnesota 55455, United States
‡Environmental Molecular Sciences Laboratory, Pacific Northwest National Laboratory, Richland, Washington 99354, United States
§Department of Chemistry, The Johns Hopkins University, Baltimore, Maryland 21218, United States
⊥Department of Chemistry and Biochemistry, University of Maryland, Baltimore County, Baltimore, Maryland 21250, United States
∥Department of Chemistry, University of Wisconsin—Madison, Madison, Wisconsin 53706, United States

Ⓢ *Supporting Information*

ABSTRACT: As-synthesized malic acid carbon dots are found to possess photoblinking properties that are outstanding and superior compared to those of conventional dyes. Considering their excellent biocompatibility, malic acid carbon dots are suitable for super-resolution fluorescence localization microscopy under a variety of conditions, as we demonstrate in fixed and live trout gill epithelial cells. In addition, during imaging experiments, the so-called "excitation wavelength-dependent" emission was not observed for individual as-made malic acid carbon dots, which motivated us to develop a time-saving and high-throughput separation technique to isolate malic acid carbon dots into fractions of different particle size distributions using C_{18} reversed-phase silica gel column chromatography. This post-treatment allowed us to determine how particle size distribution influences the optical properties of malic acid carbon dot fractions, that is, optical band gap energies and photoluminescence behaviors.

KEYWORDS: *carbon dots, photoblinking, super-resolution localization microscopy, column chromatography, photoluminescence, optical band gap energy*
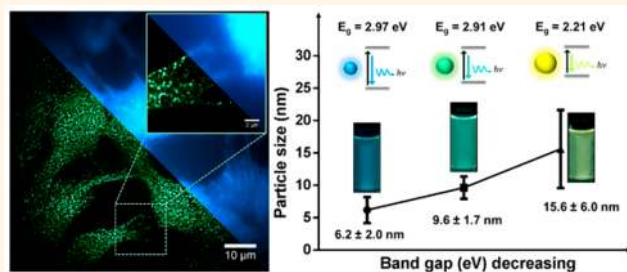
S uper-resolution fluorescence microscopy has become increasingly important for biomedical research and discovery.[1−4] Conventional fluorescence microscopy is limited by the diffraction limit of light, and imperfections in optical components further decrease spatial resolution. This results in a lateral resolution limit of 250−300 nm as determined by the Abbe criterion.[5] To obtain a resolution comparable to the size of most biomolecules (<10 nm), two major approaches are extensively used to overcome the diffraction limit: the patterned illumination-based imaging, including stimulated emission depletion (STED) microscopy and structured illumination microscopy (SIM), and single-molecule localization-based imaging, including stochastic optical reconstruction microscopy (STORM) and photo-activated localization microscopy (PALM).[6] For the latter strategy, closely clustered fluorescent molecules are resolved by stochastically turning each molecule's signal on and off.[7,8] The

centroid of on-state molecules is mathematically determined in each imaging frame. A "super-resolution" image can then be reconstructed *via* the combination of multiple iterations. To achieve high-quality super-resolution imaging, it is crucial that photoswitchable fluorophores possess high photon yield and low on−off duty cycle.[9] A variety of organic dyes can be tuned to photoblink for super-resolution localization microscopy (SRLM), mostly requiring high-power excitation and special imaging solutions containing an oxygen scavenger and high thiol content.[10,11] Even with that, few organic fluorophores have proven to be suitable for SRLM under visible excitation and emission wavelengths. It is important to note that the high photobleaching rates of organic fluorophores severely limit the
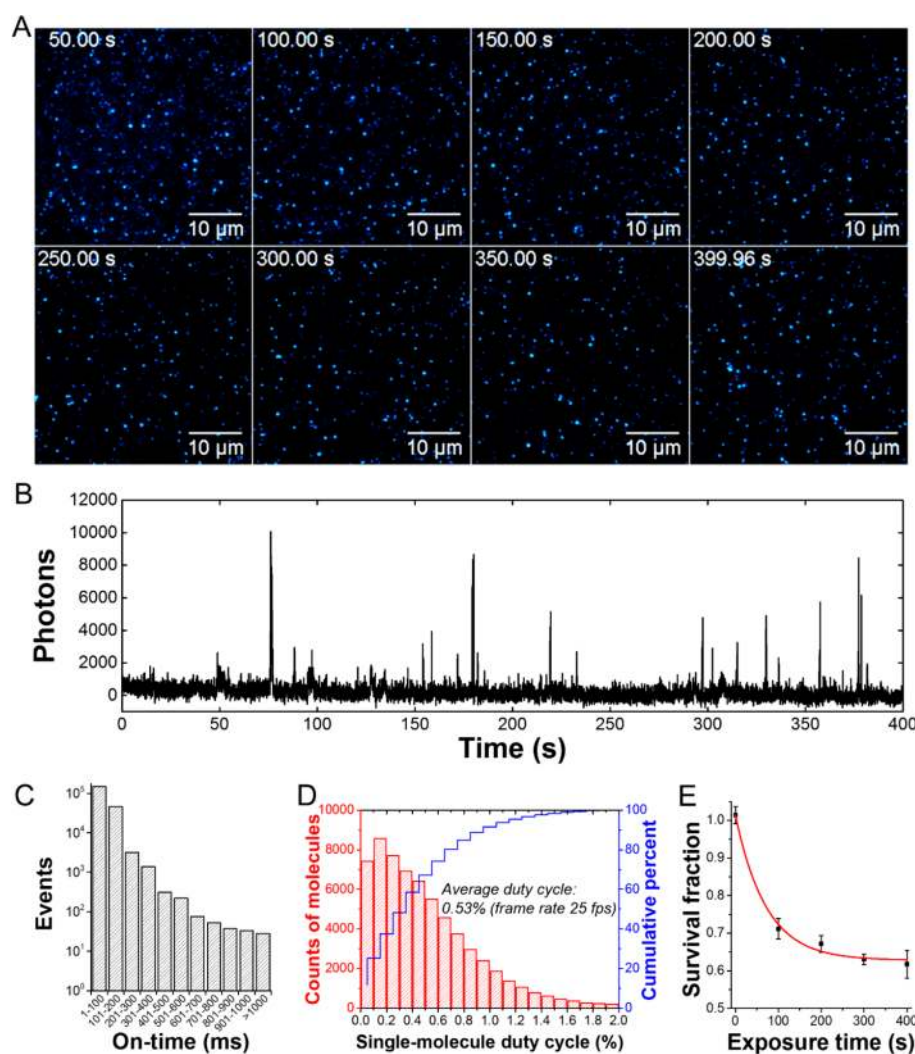
Figure 1. Characterization of individual MACDs. (A) Time-lapse fluorescence imaging of MACDs on a glass coverslip shows stochastic on and off fluorescence emission. (B) Representative fluorescence trace of an individual MACD. (C) Histogram of MACD on-time distribution. (D) Average duty cycle of MACDs, determined by summarizing a large number of single-particle blinking traces (>5000 particle traces). (E) Characterization of fluorescence emission over 400 s green excitation shows the survival fraction of MACD particles (error bars indicate the standard deviation of five independent replicates).

utility of these fluorophores in super-resolution applications, basically restricting their use to short duration applications. Hence, to advance single-molecule imaging, it is desirable to develop cost-effective and photostable fluorophores that combine spontaneous photoblinking properties with intense brightness and low photobleaching rates.

Photoluminescent zero-dimensional carbon nanostructures, including carbon dots (CDs), graphene dots, polymer dots, and nitrogen-vacancy-centered nanodiamonds, have generated great interest in many fields due to their outstanding optical properties, including their strong fluorescence, excellent water solubility, and high resistance to photobleaching.[12−17] Among these carbon-based luminescent materials, CDs have emerged as a particularly attractive option due to the availability of inexpensive carbon precursors, ease of synthesis and function-alization, and large-scale production.[18,19] CDs are characterized by broad-band optical absorption,[16,20] high emission quantum yield,[20] excellent biocompatibility,[21] and minimal environ-mental impact.[22] This combination of outstanding properties make CDs a highly promising, eco-friendly alternative to inorganic semiconductor quantum dots, which often contain

toxic heavy metals.[23,24] To date, CDs have been used in a broad range of applications including biosensing and bioimaging,[16,25] drug delivery,[26] photocatalysis,[27] patterning,[28] and photo-electronic devices.[20,29] Recently, CDs were found to be photoswitchable, which make them suitable as labeling agents for SRLM.[30−32]

Generally, CDs exhibit a quasi-spherical morphology with dimensions on the scale of 10 nm,[16,33] composed of crystalline or amorphous carbon nanostructures[34] depending on carbon-ization temperature.[35,36] CDs can be generated via a so-called "top-down" synthetic route[13,37] by breaking down bulk carbon sources such as active carbon,[38] graphite,[18,39] graphite oxide,[40,41] and carbon soot.[42,43] However, top-down methods are relatively expensive and generate less material, limiting the scale of CD production.[34] On the other hand, "bottom-up" approaches involving the assembly of the CD nanostructure using cheap molecular carbon precursors are more favorable for large-scale and high-yield production.[34,37] The choices of these small organic molecules are quite broad and include citric acid,[44] glucose,[45] chitosan,[46] vitamin C,[47] glycerol,[48] ethyl-enediaminetetraacetic acid,[49] and L-glutamic acid.[50] Bottom-up
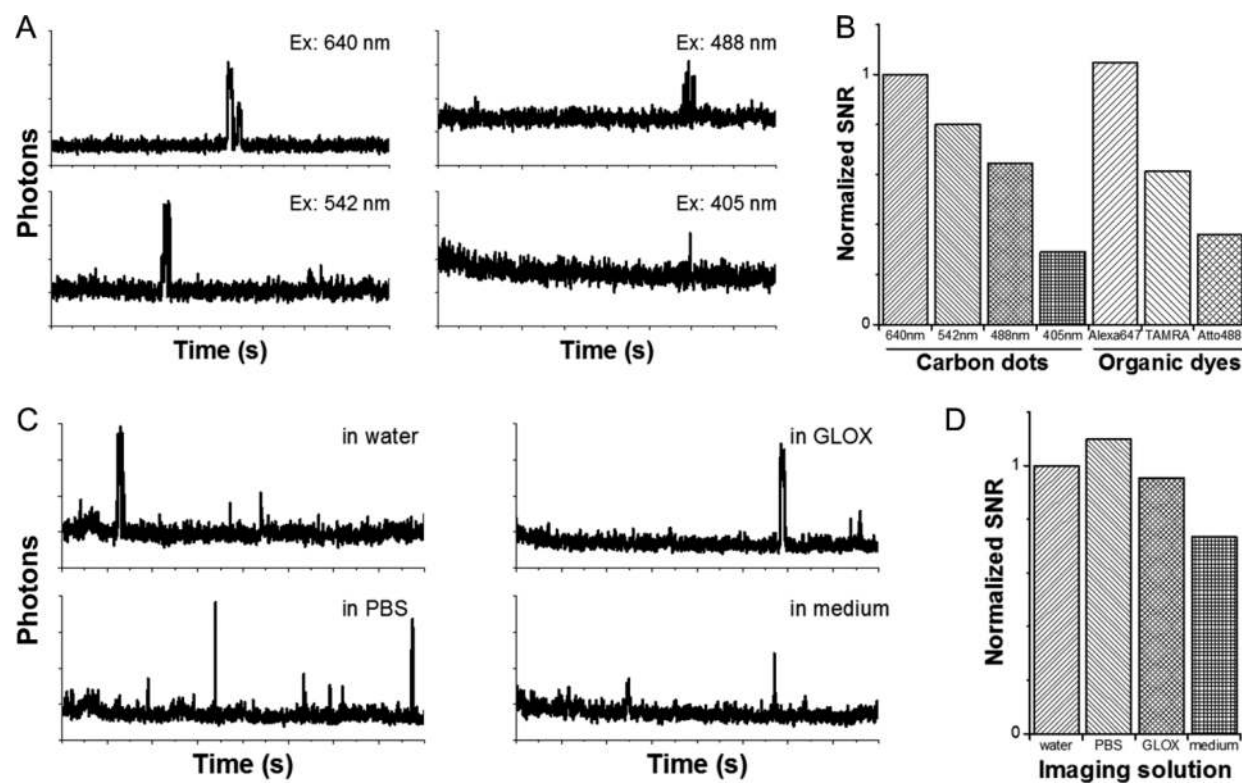
Figure 2. Characterization of the MACD SNR under different conditions. (A) Representative emission traces of MACDs in response to different excitation wavelengths. (B) SNR of MACDs under different excitation wavelengths in comparison with commonly used organic dyes under their optimal excitation wavelengths. (C) Characterization of MACD photoblinking in a variety of imaging solutions. (D) Comparison of MACD SNR in different imaging solutions.

procedures mainly involve thermal dehydration, polymerization, and carbonization of these inexpensive organic molecules.[14,34] A variety of synthesis strategies have been developed for CD fabrication, such as microwave irradiation,[51] hydrothermal carbonization,[52] pyrolysis, or thermal decomposition.[53,54] Microwave-based synthesis features advantages including strong interaction of carbon materials with electromagnetic irradiation, fast, localized heating, and energy-saving processes.[55,56] In our group, DL-malic acid (a green and inexpensive organic compound)[57] is utilized as the carbon source with ethylenediamine as the cross-linker and self-passivating agent to fabricate highly fluorescent malic acid CDs (MACDs) via a rapid microwave-assisted heating treatment.[22,58]

In recent years, there has been an exponential increase in research interest related to CD preparation and applications.[16] Nevertheless, most of the as-prepared CDs exist as a relatively complex mixture of varied components with distinct optical propeties.[59−61] Thus, the purification and/or separation of as-synthesized CDs is essential to probe the nature of single components.[19,59] In this respect, chromatographic purification has been used as an effective method to separate carbon-based photoluminescent materials.[52,62] For instance, Ding et al. employed silica column chromatography to fractionate as-made CDs based on their degree of oxidation. Though the separation results were quite impressive, the process took more than 10 h due to the high affinity of CDs toward commonly used silica gel.[52,62] High-performance liquid chromatography (HPLC) has also found favor with CD researchers as a highly efficient option for separation. Vinci et al. utilized anion-exchange HPLC (AE-HPLC) to separate as-synthesized CDs

generated from graphite nanofibers and confirmed that the emission wavelength of CD fractions was dependent on the NP size rather than the excitation wavelength.[60,63] However, AE-HPLC is more suitable to separate charged CDs produced by microwave synthesis from acidic rather than neutral small-molecule precursors.[22,59] AE-HPLC columns are also expensive. To overcome these drawbacks, Gong and co-workers applied reversed-phase HPLC (RP-HPLC) and achieved a rapid and effective separation for hollow carbon nanoparticles.[64] The isolated fractions gave off blue, green, and red fluorescence emission, which was related to the carbon shell thickness. Although RP-HPLC seems to be an ideal option, the low output that results from the limited HPLC injection volume (1−20 μL) restricts the wide-scale application of this method.[59] Therefore, there is an urgent need to develop a fast, low-cost, and high-yield separation method to realize the efficient fractionation of as-prepared CD samples.

Here, we report on the photoblinking properties of our as-synthesized MACDs. With active photoblinking, burst-like photon emission, efficient cell uptake, and high biocompatibility, we show that MACDs can be an excellent nanomaterial for SRLM. Interestingly, the well-known "wavelength-dependent emission" phenomenon was not observed in single-particle imaging experiments. As such, to further explore the physiochemical properties of MACD components, we have developed a time-saving and high-throughput method to separate as-synthesized MACDs, utilizing C_{18} reverse-phased silica gel column chromatography. The MACD fractions obtained in this way exhibit wavelength-independent emission and distinct particle size distributions (PSDs). More interestingly, these MACD fractions exhibit distinct optical properties,
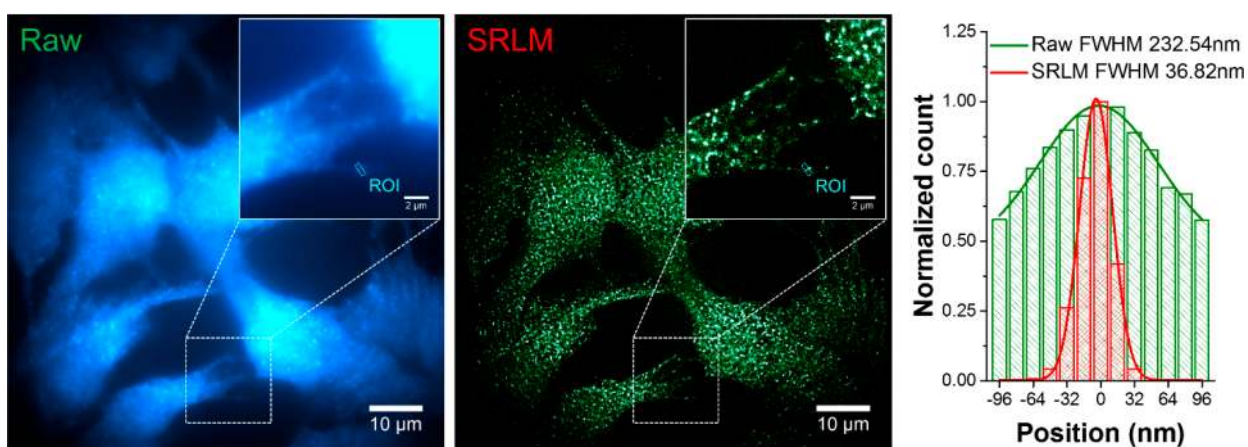
Figure 3. Super-resolution localization microscopy (SRLM) of MACDs in fixed trout epithelial gill cells. The spontaneous photoblinking of MACDs enables a significant improvement of the spatial resolution as demonstrated by the fluorescence emission profiles (right panel) of the region of interest marked by the small rectangle in the fluorescence images (fwhm, full width at half-maximum).

namely, absorption, optical band gap energy, and photoluminescence behaviors.

RESULTS AND DISCUSSION

Characterization of MACD Photoblinking. At the single-particle level, the fluorescence on−off activity of MACDs was found to be stochastic and intermittent. As shown in Figure 1A and Movie S1, the bright spots (MACDs in the on-state) were randomly distributed at different time points throughout the imaging session. In the time domain, the fluorescence trace of single MACDs further validates the stochastic nature of MACD emission (Figure 1B). The photon burst of single MACDs occurs on the millisecond level time scale, facilitating clear identification of each emission event. Under green laser excitation, the on-time of MACD photon burst is highly uniform, where over 95% of blinking events occur within 200 ms and ∼75% of events occur within 100 ms (Figure 1C). The average duty cycle of the MACDs was determined to be 0.53% (Figure 1D), consistent with a previous report.[31] Moreover, MACDs exhibited excellent photostability, as more than 60% of the particles were still fluorescent after 400 s of high-power excitation (>0.5 kW/cm^2) (Figure 1E). This set of results demonstrates the active photoblinking of the as-made MACDs and quantitatively characterizes their low duty cycle and superior photostability, identifying them as promising materials for SRLM.

To better utilize MACDs as an advanced class of imaging materials, we determined the signal-to-noise ratio (SNR) of MACDs under different conditions. First, we found that the original MACD samples responded to a broad range of excitation wavelengths, under which active photoblinking was universally observed (Figure 2A). Interestingly, a comparison of images taken from different emission channels (*e.g.*, the green and red channels) showed that the so-called "excitation wavelength-dependent" emission was not observed for individual MACDs but originated from different particles, each emitting at a different excitation wavelength. Considering our synthesis strategy, the as-synthesized MACDs were a relatively complex mixture composed of nonuniformly sized MACD particles.[22,60,65] The single-particle SNR values of these different components display a trend with higher values at the red excitation wavelength ("red particles") and lower values at the blue excitation wavelength ("blue particles") (Figure 2B).

Further, the SNR of MACDs with specific excitation wavelengths was compared with those of commonly used organic dyes in SRLM, such as Atto488 and TAMRA. The results demonstrate that MACDs have comparable, if not better, SNR over its counterparts in the chosen emission ranges (Figure 2B). The SNR of MACDs is slightly inferior to that of Alexa647 in the far-red emission range, which might be due to the low yield of red emission MACDs and cross-talk emission from other MACD components. In addition, we measured the photoblinking SNR of MACDs within different imaging solutions at the single-particle level. In conventional SRLM, a special buffer (*e.g.*, glucose-oxidase-containing solution, GLOX) is often required to reduce the dissolved oxygen level and stabilize the excited electrons in the triplet state for a long dark-state time. In contrast, the MACD's photoblinking was observed ubiquitously in a variety of imaging solutions (Figure 2C), indicating a distinctive photoblinking mechanism, different from commonly used organic dyes. Although the SNR of MACDs was negatively impacted by the complexity of the solution (a low value obtained from cell culture medium, Figure 2D), a sufficient SNR value (>15) could be achieved in all the tested solutions, making it possible to apply MACDs in various imaging environments, including live-cell imaging.

Application of MACDs in Super-resolution Localization Imaging. The MACD's photoblinking properties (low duty cycle, high photostability, and buffer-independent blinking) make them an excellent candidate for biological imaging. In light of these findings, the biocompatibility of MACDs was examined in a rainbow trout gill epithelial cell line. Cell viability was impacted only at a relatively high MACD dose (5 mg/mL), where an approximate 20% decrease in cell viability was detected 24 h post-exposure (Figure S1A), probably due to the impact of the overload of MACDs on cell proliferation through interaction with intracellular organelles and biomolecules. In addition, single-molecule fluorescence *in situ* hybridization was used to quantify gene expression at the single cell level, as particle uptake can be highly variable between cells, and substantial changes can occur at low uptake before irreversible cell death takes place.[66] In this set of experiments, we quantified mRNA copies of the stress-sensing protein p53 in response to MACDs as well as commercially available CdSe quantum dots (QDs) for comparison. After exposure to 5 μg/mL MACDs or QDs for 24 h, the gene
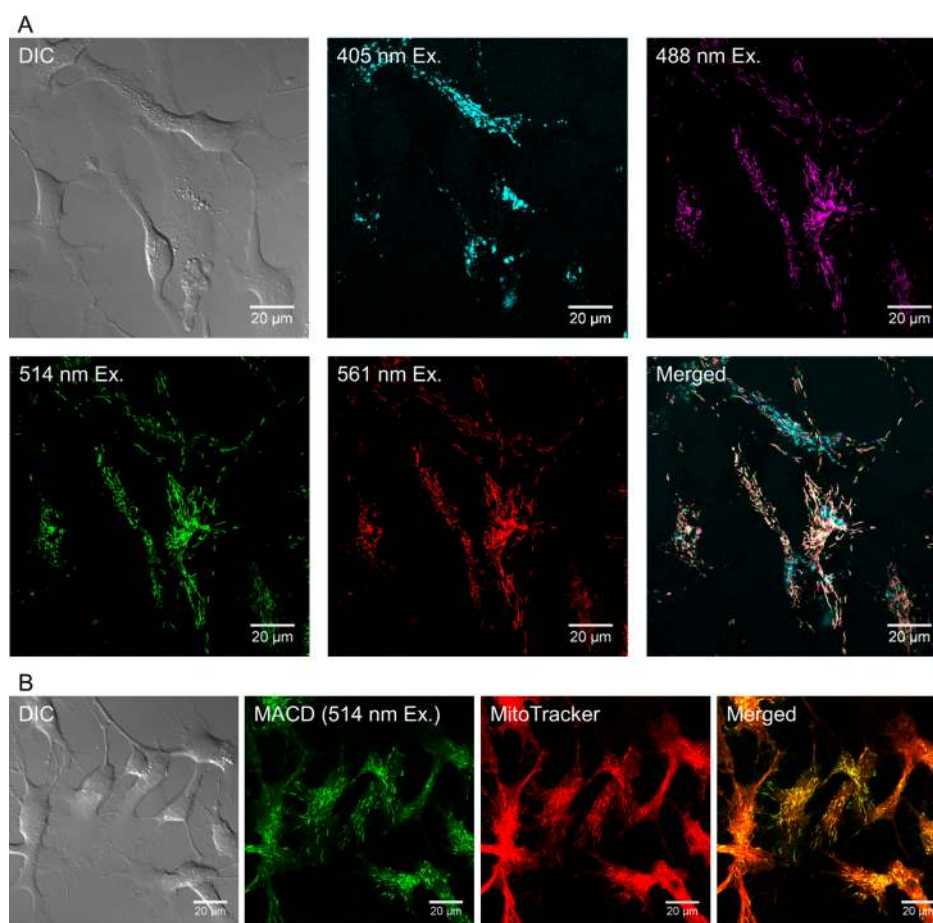
Figure 4. Distribution of MACDs in live trout gill epithelial cells. (A) MACDs with different sizes, corresponding to excitation wavelengths 488, 514, and 561 nm, were found to localize at the same intracellular compartments, whereas MACDs that were excited with 405 nm were found to localize at different compartments. (B) Green-to-yellow MACDs (with excitation wavelength ≥488 nm) were found to be present mainly in mitochondria, as determined by their colocalization with MitoTracker.

expression level of p53 in the gill cells showed detectable increase compared to that in the control group (Figure S1B). However, the expression level of p53 in cells exposed to MACDs was lower than the expression levels in cells exposed to CdSe QDs (∼30% less in copy number per cell). Hence, MACDs exhibit an overall satisfactory biocompatibility and are a promising alternative to Cd-based QDs for bioimaging experiments.

According to the Nyquist−Shannon theorem,[67] the low on−off duty cycle of MACDs makes it possible to identify ∼200 particles within a diffraction-limited area (∼250 nm). However, the spatial resolution is also constrained by localization error. Based on the Gaussian point spread function,[68] the standard error of localization using MACDs was determined to be ∼15 nm in cultured cells. Hence, the theoretical imaging resolution using green-to-yellow MACDs could reach 30 nm. SRLM was then performed both in fixed and live cells. As we demonstrate in fixed gill cells, the active photoblinking of MACDs enables a higher resolution imaging of the particles in the intracellular environment (Movie S2). As shown in Figure 3, an object with an apparent size of over 230 nm in the raw wide-field image was revealed to be around 36 nm by SRLM.

Because MACDs show sufficient blinking activity in different solutions and do not require a special buffer, the uptake and MACD internalization by live gill cells could be imaged with SRLM, as well. We observed a highly efficient uptake of

MACDs by live cells (Figure S2A and Movie S3). Interestingly, the as-synthesized MACDs exhibited two distinct intracellular distribution patterns under different excitation wavelengths. The green-to-yellow MACDs (Figure 4A, representative excitation by 488, 514, and 561 nm) show an interesting, filament-like distribution inside live cells, which is different from the distribution of blue-to-cyan MACDs (Figure 4A, representative excitation by 405 nm), as well as the distribution of MACDs in fixed cells (Figure 3). To minimize phototoxicity to living cells and lay the foundation for future applications, we focused the subsequent live-cell imaging on the green-to-yellow MACDs. The diameter of these MACD-associated structures is no more than 100 nm (Figure S3A). The improved spatial resolution also helps to distinguish closely aligned structures within a diffraction-limited area (Figure S3B). After a number of organelle-specific dyes were tested, the side-by-side comparison of live cells exposed to MACDs and MitoTracker showed a clear colocalization pattern that indicates the accumulation of MACDs in or on mitochondria (Figure 4B). Moreover, we observed directional movement of the MACD-associated mitochondria in live cells (Figure S2B and Movie S4), suggesting the transport of mitochondria-associated MACDs along the cytoskeleton (e.g., microtubules).[69,70] These results prompt the idea that this class of MACDs could be further explored as an efficient live-cell delivery vector
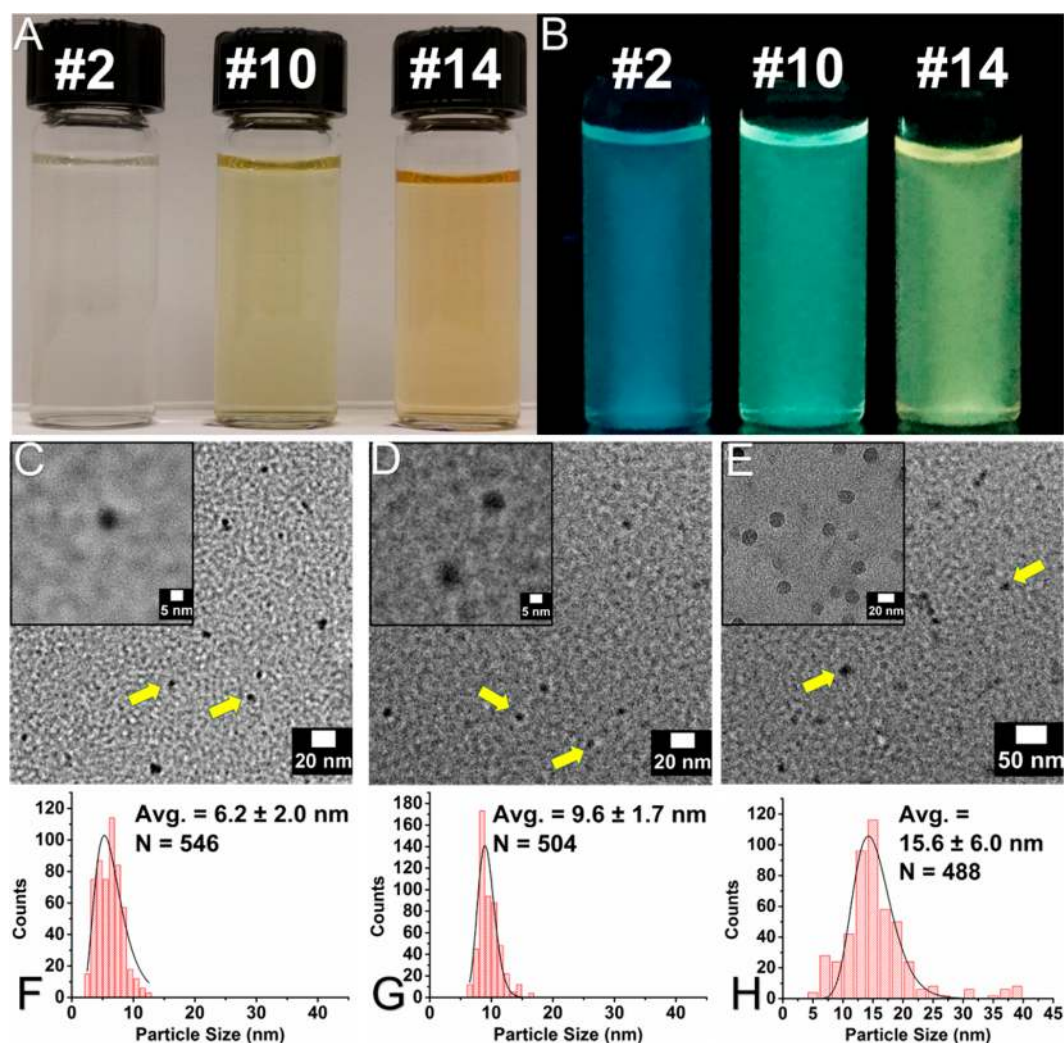
Figure 5. Photographic images of MACD fractions #2, #10, and #14 under (A) room light condition and (B) 365 nm UV illumination. TEM images of MACD fractions (C) #2, (D) #10, and (E) #14 (inset scale bar: 5, 5, and 20 nm, respectively). Corresponding PSD for MACD fractions (F) #2, (G) #10, and (H) #14, determined by ImageJ analysis of TEM images.

and mitochondria-targeting tool without further nanoparticle surface modification.

MACD Separation and Characterization of MACD Fractions. As observed in previous experiments when we tried to determine the SNR values of as-synthesized MACDs, the fluorescence emission of individual MACD particles was found to be invariant as the excitation wavelength was changed. Carbon dots are often acclaimed for their so-called "excitation-dependent emission", so this unexpected phenomenon motivated us to separate the as-synthesized MACDs into distinct fluorescent components. To combine the advantages of the traditional silica gel column chromatography and RP-HPLC as mentioned before, we employed C_{18} reversed-phase column chromatography, as shown in Scheme S1. The general setup is quite similar to that of a traditional silica gel column, but we utilized C_{18} reversed-phase silica gel as the stationary phase and a mixture of water and methanol as the mobile phase. The entire separation process (fully described in the Materials and Methods section) was accomplished in less than 3 h, remarkably time-saving compared to the traditional silica column chromatography that took more than 10 h.[52] In addition, by virtue of the large sample loading capacity, we were able to separate at least 200 mg of as-synthesized MACDs in

one single batch. As such, the output of each fraction was up to 5 mg, higher than HPLC separation yield (a few microliters, quantities of which are too small for characterization).[59] Taking advantage of this time-saving and higher throughput separation method, we obtained 24 MACD fractions (Figure S4), and three of them (i.e., fractions #2, #10, and #14) were chosen for further analysis because they were collected from three distinctive color regions visible following column chromatography. Also, their concentrations were high enough to yield bright fluorescence under a 365 nm UV lamp, representing the most promising fluorescence properties among the 24 fractions.

As shown in Figure 5A, if exposed to room light, the aqueous solutions of these three fractions appear pale yellow, yellow, and brown. These same three fractions exposed to long-wavelength UV illumination (365 nm) fluoresced blue, cyan, and greenish yellow (Figure 5B). Transmission electron microscopy (TEM) was applied to probe the size and morphology of these three MACD fractions. In Figure 5C−E, these well-dispersed MACD fractions exhibit clear circular outlines without severe agglomeration. PSDs were obtained based on these TEM images (∼500 particles counted). It was assumed that the sizes of each fraction were normally distributed, so the distribution histograms were fit with a log-
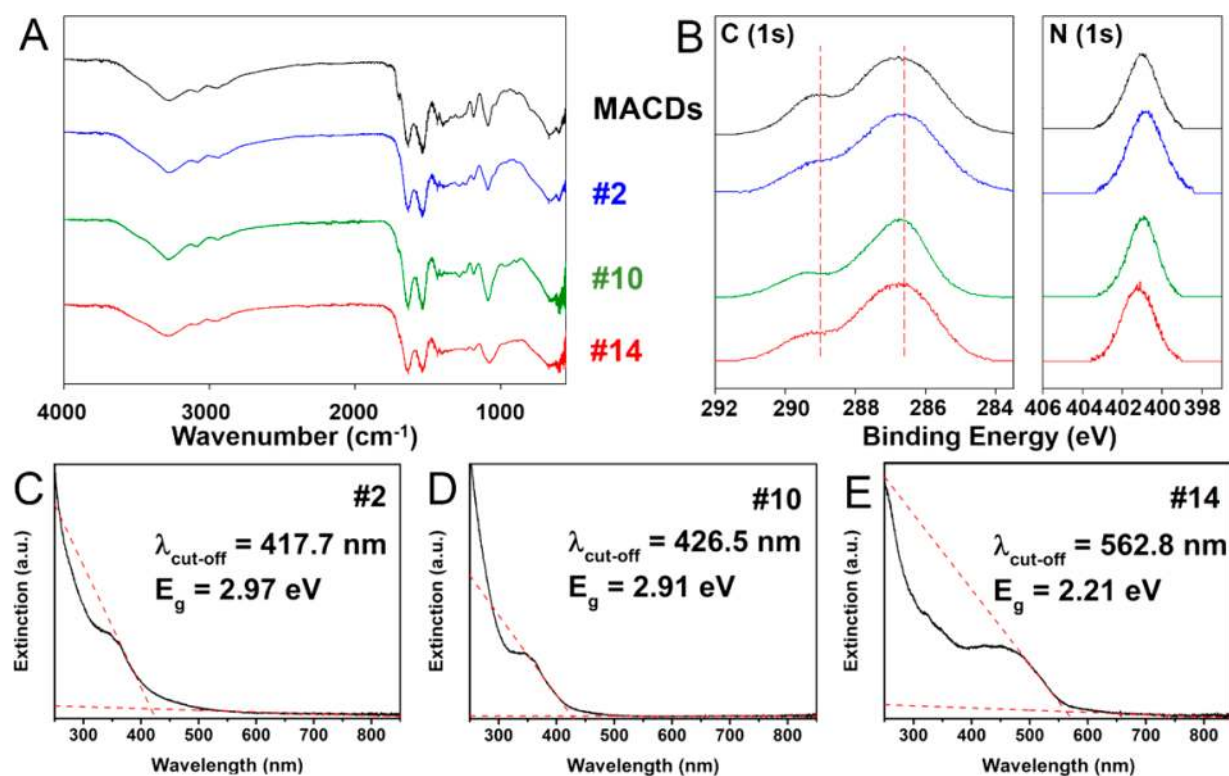
Figure 6. (A) ATR-FTIR spectroscopy and (B) XPS of unseparated MACDs (black) and MACD fraction #2 (red), #10 (green), and #14 (blue). UV−vis extinction spectra of MACD fraction: (C) #2, (D) #10, and (E) #14.

normal function to estimate the mean size of each fraction using the peak analyzer function in OriginPro 9.0. The results are displayed in Figure 5F−H, showing that MACD fraction #2 is ∼6.2 ± 2.0 nm, #10 is ∼9.2 ± 1.7 nm, and #14 is 15.6 ± 6.0 nm. It is discernible that the log-normal peak is shifting to the right, indicating an increase in particle size. The PSDs of each fraction were also statistically analyzed using one-way ANOVA multicomparison, processed by GraphPad Prism 6 (Figure S6), with significance level indicated by asterisks (*$p < 0.05$, **$p < 0.01$, ***$p < 0.001$, and ****$p < 0.0001$). Based on this analysis, the MACD fractions' PSDs were determined to be significantly different from one another. To confirm this finding, we used dynamic light scattering (DLS) to analyze the size of the MACDs in each fraction in aqueous suspension. As shown in Figure S7, the change in the PSDs between the three fractions are clear in the DLS data and are in agreement with the TEM results. We are therefore confident that the size of the MACD fractions increased when we gradually lowered the water percentage, that is, decreased the polarity of mobile phase, in the C_{18} reversed-phase column chromatography.

To assess the chemical composition of the three MACD fractions, we employed attenuated total reflectance Fourier transform infrared (ATR-FTIR) spectroscopy and X-ray photoelectron spectroscopy (XPS). IR analysis of the as-synthesized MACDs and each of the fractions are shown in Figure 6A. Each CD fraction exhibits an infrared spectrum characteristic of malic acid carbon dots. N−H, O−H, and C−H stretching bands are observed at 3280, 3080, and 2950 cm^{-1}, respectively.[71] Peaks at 1702 and 1640 cm^{-1} indicate C=O stretching modes,[72] with characteristic N−H bending and C−O stretching modes observed at 1540 and 1090 cm^{-1}, respectively.[71] Moreover, the relative intensity of these various peaks in the ATR-FTIR are observed to be virtually identical

among each of the three fractions, suggesting that the chemical bonding remains constant. XPS analysis of MACD parent batch and fractions revealed the presence of C, N, and O in all samples. Si contamination was observed in some samples, which can reasonably be assumed to have been introduced when the CD fractions were scraped off from the sides of glassware during synthesis, and for this reason, the O (1s) regions are not shown. To avoid Si contamination in the future, freeze-drying will be used instead of rotary evaporation. The C (1s) regions for the parent MACD and each one of the three CD fractions were found to be qualitatively similar, consisting of a broad peak at 286.7 eV, composed of contributions from C−C/C=C/C=O and C−N species as well as a lower intensity (roughly half) peak at 289.2 eV associated with O−C=O species.[73,74] Component fitting of the C (1s) region was not deemed appropriate due to the multiple carbon bonding environments present in the C (1s) envelope. The N (1s) region of the parent MACD and each one of the three CD fractions are characterized by a single broad peak at ≈401 eV in all samples. The broad similarities observed for both the ATR-FTIR and XPS of the three fractions indicate that there are no significant differences in the nature or relative concentration of chemical functionality among the three MACD fractions.

Optical Properties of MACD Fractions. Figure 6C−E exhibits the UV−vis extinction spectra of all separated MACD fractions. Both fractions #2 and #10 exhibit intense extinction features around 350 nm, usually assigned to n−π* transitions for nitrogen-doped CDs.[72] Interestingly, a well-resolved extinction shoulder is observed at ∼470 nm in fraction #14. Such a red shift is typically related to the narrowing of the electronic band gap and is often found for long-wavelength emissive CDs.[61,72] To confirm this, we calculated the optical band gap energy (E_g) of the three fractions using the equation
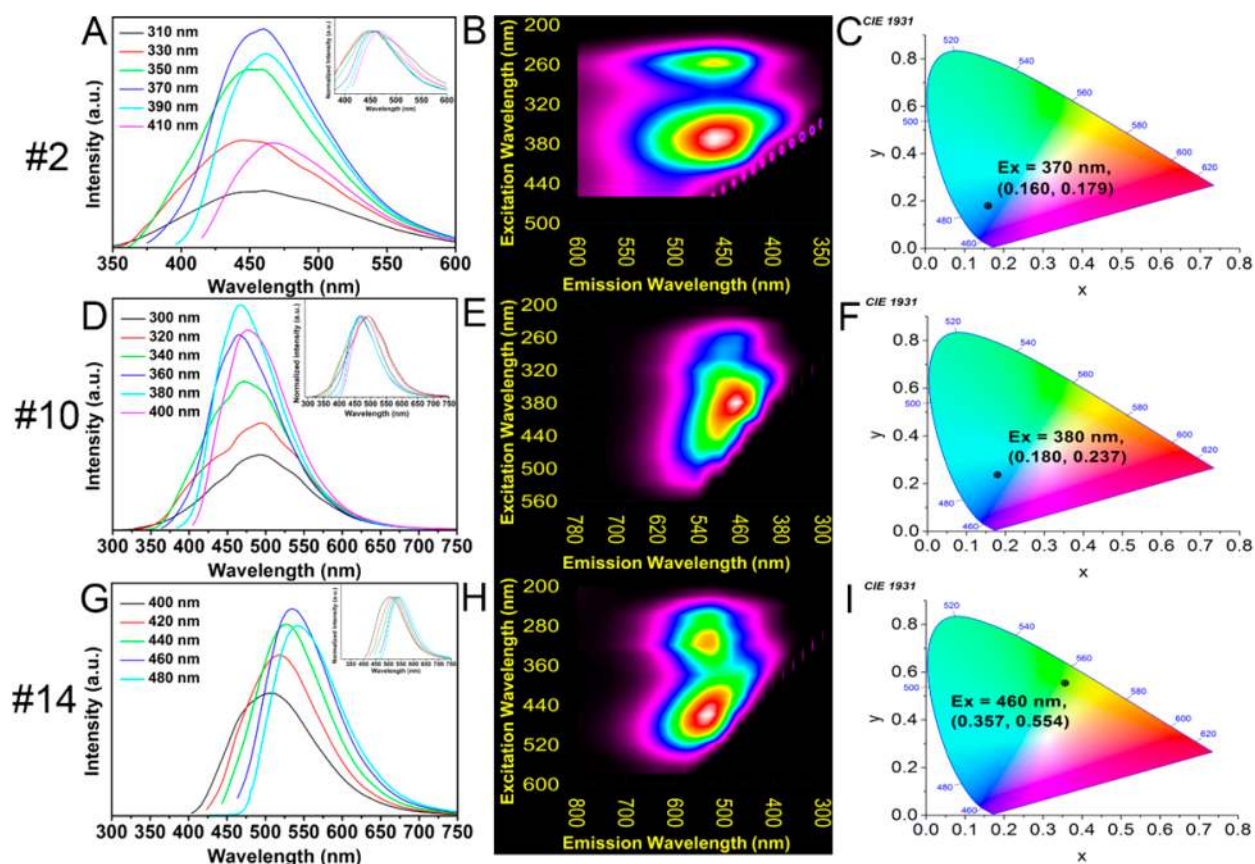
Figure 7. Fluorescence properties of MACD fractions. Top panel, fraction #2: (A) fluorescence emission under varied excitation, with normalized spectrum embedded; (B) 2D excitation−emission matrix; and (C) CIE 1931 color coordinates. Middle panel, fraction #10: (D) fluorescence emission under varied excitation, with normalized spectrum embedded; (E) 2D excitation−emission matrix; and (F) CIE 1931 color coordinates. Bottom panel, fraction #14: (G) fluorescence emission under varied excitation, with normalized spectrum embedded; (H) 2D excitation−emission matrix; and (I) CIE 1931 color coordinates.

$E_g = hc/\lambda_{cutoff}$ where h refers to the Plank constant (6.626×10^{-34} J·s), c is the speed of light (3.0×10^8 m/s), and λ_{cutoff} (in nm $\times 10^{-9}$ m) indicates the onset value of the first excitonic absorption band, with the conversion factor of 1 eV equaling 1.6×10^{-9} J.[75,76] The calculated E_g values are 2.97 eV (#2), 2.91 eV (#10), and 2.21 eV (#14), along with the increasing fraction PSDs (namely, 6.2 ± 2.0, 9.2 ± 1.7, and 15.6 ± 6.0 nm, respectively), which demonstrates how the PSD impacts the band gap energies of fractions. In addition, we systematically investigated the photoluminescent properties of MACD fractions, as illustrated by Figure 7 and Figures S8 and S9. We excited fraction #2 with a series of wavelengths ranging from 310 to 410 nm in 20 nm increments. The resulting (normalized) fluorescence emission data are shown in Figure 7A. Compared to the spectra of crude MACDs (included in Scheme S1),[22] there is no remarkable shift in the emission peak position, which is around 460 nm. The maximum emission intensity was observed at $\lambda_{ex} = 370$ nm, with a fwhm of 96 nm. A prominent luminescence center can be observed at *ca.* (371.3 and 458.7 nm) in the 2D excitation−emission matrix (EEM) (Figure 7B and Figure S9A) and 3D EEM (Figure S8A), with a Stokes shift as large as 16 822 cm^{-1}. The corresponding color coordinates (under 370 nm excitation) were calculated to be (0.160, 0.179), located within the blue region of the CIE 1931 chromaticity diagram (Figure 7C). The quantum yield (QY) of fraction #2 was measured to be as high as 30.0% using an integration sphere. For the analysis of the fluorescence lifetime,

the fluorescence decay of MACD fraction #2 was fitted with a multiexponential function (Figure S8B) to minimize deviation from the exponential fit function. This fit was further examined by residual analysis. The reduced χ^2 value of 0.987 is reasonable ($0.9 < \chi^2 < 1.2$), and residuals are distributed around zero almost symmetrically, indicative of a justifiable fitting.[77,78] Thus, the average fluorescence lifetime was extrapolated to be 6.48 ± 0.10 ns, comparable to that of commercially available fluorophores (*e.g.*, fluorescein and rhodamine).[79] The fluorescence properties of MACD fractions #10 and #14 were investigated in a similar manner. For fraction #10, the emission peak can be found at ~470 nm, achieving maximum intensity if excited by 380 nm (Figure 7D, peak width at half-max ~100 nm), leading to a bright fluorescence center at *ca.* (380.3 and 468.3 nm) in EEM (Figure 7E and Figures S8C and S9B) and a Stokes shift of 4959 cm^{-1}. The CIE 1931 coordinates of (0.180, 0.237) achieve a position in the cyan region of the color space (Figure 7F). The QY was determined to be 24.0%, with a lifetime of 7.14 ± 0.63 ns (Figure S8D). For fraction #14, the excitation-independent emission peak can be identified at 550 nm with a fwhm of *ca.* 104 nm under excitation of 460 nm (Figure 7G). Thus, a global photoluminescence center can be observed at about 460.0 and 523.7 nm (Figure 7H and Figures S8E and S9C). Accordingly, the Stokes shift decreased to 2644.3 cm^{-1}. The color of MACD fraction #14 can be defined as greenish yellow (0.357, 0.554) by CIE 1931 colorimetry (Figure 7I). Correspondingly, the calculated QY was 27.6%,

and the average lifetime was 4.25 ± 0.09 ns (Figure S8F). So, MACD fractions do not exhibit wavelength-dependent emission, in contrast to unseparated MACDs.[22] This fraction is particularly important because it represents a carbon dot population that can be used with visible, rather than UV, excitation. It is noteworthy to mention that, along with the increasing PSD, the corresponding emission of MACD fractions is red-shifted from blue to cyan and to greenish yellow, indicating that the as-prepared MACD fluorescence properties are size-dependent, consistent with other published studies.[19,60,80]

CONCLUSIONS

In summary, the as-synthesized MACDs are found to be actively photoswitchable, characterized by low duty cycle and excellent photostability. Furthermore, MACDs exhibited satisfying signal-to-noise ratio in different imaging buffer solutions. Due to these prominent and superior photoblinking properties, MACDs are shown to exhibit enhanced spatial resolution in super-resolution localization imaging experiments. To investigate the fluorescent components within as-synthesized MACDs, we developed an efficient separation method using C_{18} reversed-phase silica gel column chromatography. This approach enables us to achieve a high product output, as can be achieved with traditional silica gel column chromatography, on a time scale commensurate with HPLC. The MACD fractions showed distinct PSDs, determined by both TEM and DLS, despite having indistinguishable chemical composition. Interestingly, the optical band gap energies of MACD fractions were found to decrease with the increasing PSD, and the fluorescence of fractions is not excitation-dependent, but PSD-related, red-shifting from blue to cyan to yellowish green as the PSDs increase from 6.2 ± 2.0 to 9.2 ± 1.7 to 15.6 ± 6.0 nm.

MATERIALS AND METHODS

Materials. All materials were used as received, without further purification. DL-malic acid (MA, ReagentPlus, ≥99%), ethylenediamine (ReagentPlus, ≥99%), and C_{18} reversed-phase silica gel (for column chromatography, fully end-capped) were purchased from Sigma-Aldrich. The Biotech cellulose ester membrane (MWCO 100−500 D) was obtained from Spectrum Laboratories. Deionized water was produced by a Millipore Milli-Q system (Billerica, MA) and used for all experiments.

MACD Synthesis. We synthesized the MACDs based on our previous work.[22] Briefly, a 4 mol/L aqueous malic acid stock solution was prepared in advance. Four milliliters of this stock solution was transferred into a 100 mL beaker, and then 1080 μL of ethylenediamine was added. The reaction was completed within 1 min as heat was released, and a homogeneous solution was formed. The mixture was stirred for 30 min and allowed to cool. Then, the colorless transparent mixture was transferred to a domestic microwave oven and heated at 360 W for 3 min. The resultant dark brown foamy solid was cooled in a fume hood for 20 min before 10 mL of MQ water was added into the beaker. The dark brown transparent solution thus obtained was dialyzed for 24 h to remove unreacted precursors. Then, rotary evaporation was used to remove most of the water from the solution, leaving behind a dark brown sticky solid product at the bottom. Further lyophilization was completed in a freeze-dryer (Labconco FreeZone 4.5 L benchtop freeze-dry system) for 16 h.

Characterization of the MACD Photoblinking. To characterize the photoblinking properties of MACDs, a low concentration solution (0.5 μg MACD/mL, to avoid having multiple particles in a single imaging pixel) was used to achieve uniform dispersion of particles onto a clean #1.5 coverslip. The exposure experiments and SRLM were performed with a home-built single-molecule fluorescence imaging system based on an Olympus IX71 microscope. High-power solid-state

laser sources (>0.1 kW/cm^2) were used to excite MACDs at different wavelengths (405, 488, 542, 642 nm). The emitted fluorescence was collected with a 100× oil immersion objective (NA = 1.4) and imaged with an EMCCD camera (Andor iXon 897). The raw images were stored as 16-bit 512 × 512 files (pixel size 160 nm). In general, a 600 s time series was taken at the frame rate of 25 fps. The photoblinking of MACDs became stable after 200 s excitation, and so the subsequent 400 s data was used in post-processing. From such series of exposures, the duty cycle of a single particle was determined as the proportion of image frames with fluorescence emission events. The signal-to-noise ratio was defined as the ratio of the mean emission intensity of single MACD to the background fluctuation: $\text{SNR} = \frac{I_s - I_b}{\sigma_b}$, where I_s is the emission intensity of single MACD, I_b is the mean intensity of the background, and σ_b is the standard deviation/fluctuation of the background. I_b and σ_b were obtained from pixel traces without MACDs, and I_s of MACD emission events was defined as 5 times the σ_b value over the I_b value in pixel traces with MACDs. Post-processing was conducted with MATLAB and OriginPro software. All imaging buffers were freshly prepared before each experiment. The GLOX solution contained 50 mM Tris (pH 8.0), 10 mM NaCl, 10% glucose, 560 μg/mL glucose oxidase (Sigma, G2133), 34 μg/mL catalase (Sigma, C3155), and 1% 2-mercaptoethanol.

Cell Imaging and Cytotoxicity Analysis. *Oncorhynchus mykiss* (rainbow trout) epithelial gill cells (ATCC, CRL-2523) were routinely cultured in Leibovitz's L-15 media supplemented with 10% fetal bovine serum and 1% penicillin−streptomycin. Cells were grown at 19 °C in ambient atmosphere. Before imaging, cells were incubated with 5 μg/mL MACDs for 2 h. Prior to live-cell imaging, culture medium was replaced with a phenol-red free imaging solution (Thermo Fisher Scientific, A14291DJ). In SRLM, a Gaussian mask-function-based single-molecule localization algorithm was used, for which a detailed description can be found in our previous studies.[81,82] In brief, image stacks were taken under 542 nm excitation (50−100 W/cm^2) and 25 Hz (8000−10 000 frames). Raw images were first smoothed with a LoG filter, followed by identification of local maxima. Based on the local maxima, fluorescence emission was determined while a blinking event was defined as the signal above a threshold of 5 times the standard deviation of the background fluctuation. The localization error was calculated according to the equation:

$$\langle (\Delta x)^2 \rangle = \frac{s^2 + a^2/12}{N} + \frac{8\pi s^4 b^2}{a^2 N^2}$$

where s is the standard deviation of the Gaussian point spread funtion, a is the pixel size, b is the background noise, and N is the collected photons.[68] For MACDs under 520−560 nm excitation, the localization error was determined to be ∼15 nm, and the resolution of reconstructed images was set to 30 nm. Movies of intracellular movement of MACDs were made of selected frames from the whole image stacks. The intracellular localization experiments (Figure 4) were performed on a Zeiss LSM 710 confocal system and using MitoTracker Deep Red (Thermo Fisher Scientific, M22426).

Upon different treatment conditions, the cell viability was determined with the MTS proliferation assay (Promega, G3580). Single-molecule fluorescence *in situ* hybridization (smFISH) was used to evaluate the impact of MACDs and CdSe quantum dots to the expression level of the p53 gene. In brief, 80−90% confluent cells were exposed to 5 μg/mL MACDs for 24 h, followed by fixation with 4% paraformaldehyde and permeabilization with 70% ethanol. The hybridization step was performed with 5 nM oligonucleotide probes, 10% dextran sulfate, 10% formamide, and 2× saline-sodium citrate at 37 °C overnight. The cell nuclei were counterstained with DAPI. For each field of view, a z-stack spanning 7−10 μm was taken, and the location of each transcript was identified by a maximum intensity projection. The quantification of RNA copies in each single cell was performed with customized MATLAB scripts. The sequence information on the smFISH probes is provided in Table S1.

MACD Separation by C_{18} Reversed-Phase Silica Gel Column Chromatography. As demonstrated by Scheme S1, 1 mL of highly concentrated carbon dot solution (200 mg/mL) was prepared for

column chromatography. During the separation process, the fluorescence of each fraction was examined by a portable UV lamp (365 nm). Pure MQ water was used as the first mobile phase until the blue fractions of carbon dots had completely eluted. Then, the MeOH/MQ water mixture was used as the second mobile phase with the MeOH ratio gradually increasing until pure MeOH was used as the final mobile phase (volume ratio of MeOH/MQ water starts from 1:9, MeOH% was added by 20% per 30 mL). In this way, 24 MACD fractions were obtained after the first round of separation, as shown in Figure S4. A subset of these fractions still exhibited excitation-dependent emission (Figure S5). So, to further separate fractions #10 and #14, we applied the identical method once more. These twice purified fractions were dried by rotovap into powder form for further experiments.

Material Characterization of MACDs. The particle size distribution of carbon dots was determined by TEM (FEI Tecnai G^2 F30 TEM at 300 kV) and DLS (Microtrac NANO-flex 180° DLS System). UV−vis extinction spectra were obtained using a Mikropack DH-2000 UV−vis−NIR spectrometer. Fluorescence spectra and EEMs were measured with a PTI QuantaMaster 400, equipped with a PicoMaster TCSPC steady-state and fluorescence lifetime spectrometer for lifetime analysis. Infrared spectra (ATR-FTIR) were obtained using a Thermo Scientific Nicolet iS5 FTIR spectrometer with an iD5 attenuated total reflectance attachment. Spectra were obtained with 64 scans using 0.8 cm^{-1} resolution and a diamond crystal stage. X-ray photoelectron spectra of MACDs were obtained using a PHI 5600 instrument equipped with a Mg Kα flood source (1253.6 eV) and a hemispherical energy analyzer. Survey scans were taken at a pass energy of 187.85 eV with a 1.6 eV/step size and 10 sweeps. High-resolution multiplex scans of C (1s), O (1s), and N (1s) regions were taken at a source power of 300 W, with a pass energy of 5.85 eV, 0.025 eV/step, and 50 sweeps. All XPS data were analyzed using CASA XPS software. It was necessary to wash as-synthesized MACDs and some MACD fractions to remove silicon contamination which was identified in preliminary XPS measurements and was presumably introduced when the MACDs were scraped from the glassware. First, MACDs were suspended in water and subsequently centrifuged to remove silica. The supernatant was then separated and lyophilized to recover the MACDs. This significantly reduced the level of silicon contamination. MACDs were attached as a powder to double-sided copper adhesive tape, which was attached to an XPS sample stage. Due to the smaller amount of available sample (<20 mg), MACD fractions were dried after filtration onto aluminum foil, which was then adhered to the sample stage with double-sided copper adhesive tape. In these cases, a small aperture size was used for XPS analysis to avoid detecting background aluminum from the foil.

ASSOCIATED CONTENT

ⓢ Supporting Information

The Supporting Information is available free of charge on the ACS Publications website at DOI: 10.1021/acsnano.8b01619.

> Figures S1−S9, Scheme S1, and Table S1 (PDF)
>
> Movie S1: Demonstration of the *in vitro* photoblinking of MACDs (AVI)
>
> Movie S2: Demonstration of MACD photoblinking in trout gill cells (AVI)
>
> Movie S3: Demonstration of MACD uptake by live cells (AVI)
>
> Movie S4: Demonstration of MACD transport in live cells (AVI)

AUTHOR INFORMATION

Corresponding Authors

*E-mail: galya.orr@pnnl.gov

*E-mail: chaynes@umn.edu.

ORCID

Bo Zhi: 0000-0002-1918-5012
Denise N. Williams: 0000-0002-6314-2052
Richard P. Brown: 0000-0001-5145-5425
Eric S. Melby: 0000-0002-3812-2965
Robert J. Hamers: 0000-0003-3821-9625
Zeev Rosenzweig: 0000-0001-6098-3932
D. Howard Fairbrother: 0000-0003-4405-9728
Galya Orr: 0000-0002-5552-2151
Christy L. Haynes: 0000-0002-5420-5867

Present Address

#Columbia Basin College, Pasco, WA 99301, USA.

Author Contributions

¶B.Z. and Y.C. contributed equally.

Notes

The authors declare no competing financial interest.

REFERENCES

(1) Huang, B.; Bates, M.; Zhuang, X. Super-Resolution Fluorescence Microscopy. *Annu. Rev. Biochem.* **2009**, *78*, 993−1016.

(2) Sauer, M.; Heilemann, M. Single-Molecule Localization Microscopy in Eukaryotes. *Chem. Rev.* **2017**, *117*, 7478−7509.

(3) Gahlmann, A.; Moerner, W. E. Exploring Bacterial Cell Biology with Single-Molecule Tracking and Super-Resolution Imaging. *Nat. Rev. Microbiol.* **2014**, *12*, 9−22.

(4) Cui, Y.; Irudayaraj, J. Inside Single Cells: Quantitative Analysis with Advanced Optics and Nanomaterials. *Wiley Interdiscip. Rev. Nanomed. Nanobiotechnol.* **2015**, *7*, 387−407.

(5) Abbe, E. Ueber Einen Neuen Beleuchtungsapparat Am Mikroskop. *Archiv für Mikroskopische Anatomie* **1873**, *9*, 469−480.

(6) Huang, B.; Babcock, H.; Zhuang, X. Breaking the Diffraction Barrier: Super-Resolution Imaging of Cells. *Cell* **2010**, *143*, 1047−58.

(7) Rust, M. J.; Bates, M.; Zhuang, X. Sub-Diffraction-Limit Imaging by Stochastic Optical Reconstruction Microscopy (STORM). *Nat. Methods* **2006**, *3*, 793−5.

(8) Betzig, E.; Patterson, G. H.; Sougrat, R.; Lindwasser, O. W.; Olenych, S.; Bonifacino, J. S.; Davidson, M. W.; Lippincott-Schwartz, J.; Hess, H. F. Imaging Intracellular Fluorescent Proteins at Nanometer Resolution. *Science* **2006**, *313*, 1642−1645.

(9) Dempsey, G. T.; Vaughan, J. C.; Chen, K. H.; Bates, M.; Zhuang, X. Evaluation of Fluorophores for Optimal Performance in Localization-Based Super-Resolution Imaging. *Nat. Methods* **2011**, *8*, 1027−36.

(10) Vogelsang, J.; Cordes, T.; Forthmann, C.; Steinhauer, C.; Tinnefeld, P. Controlling the Fluorescence of Ordinary Oxazine Dyes for Single-Molecule Switching and Superresolution Microscopy. *Proc. Natl. Acad. Sci. U. S. A.* **2009**, *106*, 8107−12.

(11) Heilemann, M.; van de Linde, S.; Mukherjee, A.; Sauer, M. Super-Resolution Imaging with Small Organic Fluorophores. *Angew. Chem., Int. Ed.* **2009**, *48*, 6903−6908.

(12) Georgakilas, V.; Perman, J. A.; Tucek, J.; Zboril, R. Broad Family of Carbon Nanoallotropes: Classification, Chemistry, and Applications of Fullerenes, Carbon Dots, Nanotubes, Graphene, Nanodiamonds, and Combined Superstructures. *Chem. Rev.* **2015**, *115*, 4744−822.

(13) Lim, S. Y.; Shen, W.; Gao, Z. Carbon Quantum Dots and Their Applications. *Chem. Soc. Rev.* **2015**, *44*, 362−81.

(14) Liu, W. J.; Li, C.; Ren, Y. J.; Sun, X. B.; Pan, W.; Li, Y. H.; Wang, J. P.; Wang, W. J. Carbon Dots: Surface Engineering and Applications. *J. Mater. Chem. B* **2016**, *4*, 5772−5788.

(15) Zhu, S.; Song, Y.; Shao, J.; Zhao, X.; Yang, B. Non-Conjugated Polymer Dots with Crosslink-Enhanced Emission in the Absence of Fluorophore Units. *Angew. Chem., Int. Ed.* **2015**, *54*, 14626−37.

(16) Peng, Z. L.; Han, X.; Li, S. H.; Al-Youbi, A. O.; Bashammakh, A. S.; El-Shahawi, M. S.; Leblanc, R. M. Carbon Dots: Biomacromolecule Interaction, Bioimaging and Nanomedicine. *Coord. Chem. Rev.* **2017**, *343*, 256−277.

(17) Hsiao, W. W.; Hui, Y. Y.; Tsai, P. C.; Chang, H. C. Fluorescent Nanodiamond: A Versatile Tool for Long-Term Cell Tracking, Super-Resolution Imaging, and Nanoscale Temperature Sensing. *Acc. Chem. Res.* **2016**, *49*, 400−7.

(18) Wang, Y. F.; Hu, A. G. Carbon Quantum Dots: Synthesis, Properties and Applications. *J. Mater. Chem. C* **2014**, *2*, 6921−6939.

(19) Shamsipur, M.; Barati, A.; Karami, S. Long-Wavelength, Multicolor, and White-Light Emitting Carbon-Based Dots: Achievements Made, Challenges Remaining, and Applications. *Carbon* **2017**, *124*, 429−472.

(20) Wang, Y.; Kalytchuk, S.; Wang, L.; Zhovtiuk, O.; Cepe, K.; Zboril, R.; Rogach, A. L. Carbon Dot Hybrids with Oligomeric Silsesquioxane: Solid-State Luminophores with High Photoluminescence Quantum Yield and Applicability in White Light Emitting Devices. *Chem. Commun. (Cambridge, U. K.)* **2015**, *51*, 2950−3.

(21) Kalytchuk, S.; Polakova, K.; Wang, Y.; Froning, J. P.; Cepe, K.; Rogach, A. L.; Zboril, R. Carbon Dot Nanothermometry: Intracellular Photoluminescence Lifetime Thermal Sensing. *ACS Nano* **2017**, *11*, 1432−1442.

(22) Zhi, B.; Gallagher, M. J.; Frank, B. P.; Lyons, T. Y.; Qiu, T. A.; Da, J.; Mensch, A. C.; Hamers, R. J.; Rosenzweig, Z.; Fairbrother, D. H.; Haynes, C. L. Investigation of Phosphorous Doping Effects on Polymeric Carbon Dots: Fluorescence, Photostability, and Environmental Impact. *Carbon* **2018**, *129*, 438−449.

(23) Alivisatos, A. P. Semiconductor Clusters, Nanocrystals, and Quantum Dots. *Science* **1996**, *271*, 933−937.

(24) Hardman, R. A Toxicologic Review of Quantum Dots: Toxicity Depends on Physicochemical and Environmental Factors. *Environ. Health Perspect* **2006**, *114*, 165−72.

(25) Ding, C.; Zhu, A.; Tian, Y. Functional Surface Engineering of C-Dots for Fluorescent Biosensing and *in vivo* Bioimaging. *Acc. Chem. Res.* **2014**, *47*, 20−30.

(26) Feng, T.; Ai, X.; An, G.; Yang, P.; Zhao, Y. Charge-Convertible Carbon Dots for Imaging-Guided Drug Delivery with Enhanced *in vivo* Cancer Therapeutic Efficiency. *ACS Nano* **2016**, *10*, 4410−20.

(27) Hu, S.; Tian, R.; Dong, Y.; Yang, J.; Liu, J.; Chang, Q. Modulation and Effects of Surface Groups on Photoluminescence and Photocatalytic Activity of Carbon Dots. *Nanoscale* **2013**, *5*, 11665−71.

(28) Zhu, S.; Meng, Q.; Wang, L.; Zhang, J.; Song, Y.; Jin, H.; Zhang, K.; Sun, H.; Wang, H.; Yang, B. Highly Photoluminescent Carbon Dots for Multicolor Patterning, Sensors, and Bioimaging. *Angew. Chem., Int. Ed.* **2013**, *52*, 3953−7.

(29) Choi, H.; Ko, S. J.; Choi, Y.; Joo, P.; Kim, T.; Lee, B. R.; Jung, J. W.; Choi, H. J.; Cha, M.; Jeong, J. R.; Hwang, I. W.; Song, M. H.; Kim, B. S.; Kim, J. Y. Versatile Surface Plasmon Resonance of Carbon-Dot-Supported Silver Nanoparticles in Polymer Optoelectronic Devices. *Nat. Photonics* **2013**, *7*, 732−738.

(30) Chizhik, A. M.; Stein, S.; Dekaliuk, M. O.; Battle, C.; Li, W.; Huss, A.; Platen, M.; Schaap, I. A.; Gregor, I.; Demchenko, A. P.; Schmidt, C. F.; Enderlein, J.; Chizhik, A. I. Super-Resolution Optical

(31) He, H.; Liu, X.; Li, S.; Wang, X.; Wang, Q.; Li, J.; Wang, J.; Ren, H.; Ge, B.; Wang, S.; Zhang, X.; Huang, F. High-Density Super-Resolution Localization Imaging with Blinking Carbon Dots. *Anal. Chem.* **2017**, *89*, 11831−11838.

(32) Khan, S.; Verma, N. C.; Gupta, A.; Nandi, C. K. Reversible Photoswitching of Carbon Dots. *Sci. Rep.* **2015**, *5*, 11423.

(33) Sun, Y. P.; Zhou, B.; Lin, Y.; Wang, W.; Fernando, K. A.; Pathak, P.; Meziani, M. J.; Harruff, B. A.; Wang, X.; Wang, H.; Luo, P. G.; Yang, H.; Kose, M. E.; Chen, B.; Veca, L. M.; Xie, S. Y. Quantum-Sized Carbon Dots for Bright and Colorful Photoluminescence. *J. Am. Chem. Soc.* **2006**, *128*, 7756−7.

(34) Hutton, G. A. M.; Martindale, B. C. M.; Reisner, E. Carbon Dots As Photosensitisers for Solar-Driven Catalysis. *Chem. Soc. Rev.* **2017**, *46*, 6111−6123.

(35) Martindale, B. C. M.; Hutton, G. A. M.; Caputo, C. A.; Prantl, S.; Godin, R.; Durrant, J. R.; Reisner, E. Enhancing Light Absorption and Charge Transfer Efficiency in Carbon Dots through Graphitization and Core Nitrogen Doping. *Angew. Chem., Int. Ed.* **2017**, *56*, 6459−6463.

(36) Cayuela, A.; Soriano, M. L.; Carrillo-Carrion, C.; Valcarcel, M. Semiconductor and Carbon-Based Fluorescent Nanodots: The Need for Consistency. *Chem. Commun. (Cambridge, U. K.)* **2016**, *52*, 1311−26.

(37) Wu, Z. L.; Liu, Z. X.; Yuan, Y. H. Carbon Dots: Materials, Synthesis, Properties and Approaches to Long-Wavelength and Multicolor Emission. *J. Mater. Chem. B* **2017**, *5*, 3794−3809.

(38) Qiao, Z. A.; Wang, Y.; Gao, Y.; Li, H.; Dai, T.; Liu, Y.; Huo, Q. Commercially Activated Carbon As the Source for Producing Multicolor Photoluminescent Carbon Dots by Chemical Oxidation. *Chem. Commun. (Cambridge, U. K.)* **2009**, *46*, 8812−4.

(39) Ming, H.; Ma, Z.; Liu, Y.; Pan, K.; Yu, H.; Wang, F.; Kang, Z. Large Scale Electrochemical Synthesis of High Quality Carbon Nanodots and Their Photocatalytic Property. *Dalton Trans.* **2012**, *41*, 9526−31.

(40) Yeh, T. F.; Syu, J. M.; Cheng, C.; Chang, T. H.; Teng, H. S. Graphite Oxide As a Photocatalyst for Hydrogen Production from Water. *Adv. Funct. Mater.* **2010**, *20*, 2255−2262.

(41) Wang, Q.; Zheng, H.; Long, Y.; Zhang, L.; Gao, M.; Bai, W. Microwave−Hydrothermal Synthesis of Fluorescent Carbon Dots from Graphite Oxide. *Carbon* **2011**, *49*, 3134−3140.

(42) Liu, H.; Ye, T.; Mao, C. Fluorescent Carbon Nanoparticles Derived from Candle Soot. *Angew. Chem., Int. Ed.* **2007**, *46*, 6473−5.

(43) Tian, L.; Ghosh, D.; Chen, W.; Pradhan, S.; Chang, X. J.; Chen, S. W. Nanosized Carbon Particles from Natural Gas Soot. *Chem. Mater.* **2009**, *21*, 2803−2809.

(44) Zhai, X.; Zhang, P.; Liu, C.; Bai, T.; Li, W.; Dai, L.; Liu, W. Highly Luminescent Carbon Nanodots by Microwave-Assisted Pyrolysis. *Chem. Commun. (Cambridge, U. K.)* **2012**, *48*, 7955−7.

(45) Moon, B. J.; Oh, Y.; Shin, D. H.; Kim, S. J.; Lee, S. H.; Kim, T. W.; Park, M.; Bae, S. Facile and Purification-Free Synthesis of Nitrogenated Amphiphilic Graphitic Carbon Dots. *Chem. Mater.* **2016**, *28*, 1481−1488.

(46) Chowdhury, D.; Gogoi, N.; Majumdar, G. Fluorescent Carbon Dots Obtained from Chitosan Gel. *RSC Adv.* **2012**, *2*, 12156−12159.

(47) Jia, X.; Li, J.; Wang, E. One-Pot Green Synthesis of Optically pH-Sensitive Carbon Dots with Upconversion Luminescence. *Nanoscale* **2012**, *4*, 5572−5.

(48) Lai, C. W.; Hsiao, Y. H.; Peng, Y. K.; Chou, P. T. Facile Synthesis of Highly Emissive Carbon Dots from Pyrolysis of Glycerol; Gram Scale Production of Carbon Dots/mSiO₂ for Cell Imaging and Drug Release. *J. Mater. Chem.* **2012**, *22*, 14403−14409.

(49) Pan, D.; Zhang, J.; Li, Z.; Wu, C.; Yan, X.; Wu, M. Observation of pH-, Solvent-, Spin-, and Excitation-Dependent Blue Photoluminescence from Carbon Nanoparticles. *Chem. Commun. (Cambridge, U. K.)* **2010**, *46*, 3681−3.

(50) Wu, X.; Tian, F.; Wang, W.; Chen, J.; Wu, M.; Zhao, J. X. Fabrication of Highly Fluorescent Graphene Quantum Dots Using L-

Fluctuation Bio-Imaging with Dual-Color Carbon Nanodots. *Nano Lett.* **2016**, *16*, 237−42.

Glutamic Acid for *in vitro/in vivo* Imaging and Sensing. *J. Mater. Chem. C* **2013**, *1*, 4676−4684.

(51) Wu, Y.; Liu, X.; Wu, Q.; Yi, J.; Zhang, G. Carbon Nanodots-Based Fluorescent Turn-on Sensor Array for Biothiols. *Anal. Chem.* **2017**, *89*, 7084−7089.

(52) Ding, H.; Yu, S. B.; Wei, J. S.; Xiong, H. M. Full-Color Light-Emitting Carbon Dots with a Surface-State-Controlled Luminescence Mechanism. *ACS Nano* **2016**, *10*, 484−91.

(53) Wang, F.; Xie, Z.; Zhang, B.; Liu, Y.; Yang, W.; Liu, C. Y. Down-and up-Conversion Luminescent Carbon Dot Fluid: Inkjet Printing and Gel Glass Fabrication. *Nanoscale* **2014**, *6*, 3818−23.

(54) Bourlinos, A. B.; Stassinopoulos, A.; Anglos, D.; Zboril, R.; Karakassides, M.; Giannelis, E. P. Surface Functionalized Carbogenic Quantum Dots. *Small* **2008**, *4*, 455−8.

(55) Schwenke, A. M.; Hoeppener, S.; Schubert, U. S. Synthesis and Modification of Carbon Nanomaterials Utilizing Microwave Heating. *Adv. Mater.* **2015**, *27*, 4113−41.

(56) Horikoshi, S.; Serpone, N. *Microwaves in Nanoparticle Synthesis: Fundamentals and Applications*; John Wiley & Sons: New York, 2013.

(57) Panduric, N.; Salic, A.; Zelic, B. Fully Integrated Biotransformation of Fumaric Acid by Permeabilized Baker's Yeast Cells with *in situ* Separation of L-Malic Acid Using Ultrafiltration, Acidification and Electrodialysis. *Biochem. Eng. J.* **2017**, *125*, 221−229.

(58) Pham, S. N.; Kuether, J. E.; Gallagher, M. J.; Hernandez, R. T.; Williams, D. N.; Zhi, B.; Mensch, A. C.; Hamers, R. J.; Rosenzweig, Z.; Fairbrother, H.; Krause, M. O. P.; Feng, Z. V.; Haynes, C. L. Carbon Dots: A Modular Activity to Teach Fluorescence and Nanotechnology at Multiple Levels. *J. Chem. Educ.* **2017**, *94*, 1143−1149.

(59) Gong, X.; Chin Paau, M.; Hu, Q.; Shuang, S.; Dong, C.; Choi, M. M. UHPLC Combined with Mass Spectrometric Study of As-Synthesized Carbon Dots Samples. *Talanta* **2016**, *146*, 340−50.

(60) Vinci, J. C.; Ferrer, I. M.; Seedhouse, S. J.; Bourdon, A. K.; Reynard, J. M.; Foster, B. A.; Bright, F. V.; Colon, L. A. Hidden Properties of Carbon Dots Revealed after HPLC Fractionation. *J. Phys. Chem. Lett.* **2013**, *4*, 239−43.

(61) Hola, K.; Sudolska, M.; Kalytchuk, S.; Nachtigallova, D.; Rogach, A. L.; Otyepka, M.; Zboril, R. Graphitic Nitrogen Triggers Red Fluorescence in Carbon Dots. *ACS Nano* **2017**, *11*, 12402−12410.

(62) Nie, H.; Li, M. J.; Li, Q. S.; Liang, S. J.; Tan, Y. Y.; Sheng, L.; Shi, W.; Zhang, S. X. A. Carbon Dots with Continuously Tunable Full-Color Emission and Their Application in Ratiometric pH Sensing. *Chem. Mater.* **2014**, *26*, 3104−3112.

(63) Vinci, J. C.; Colon, L. A. Fractionation of Carbon-Based Nanomaterials by Anion-Exchange Hplc. *Anal. Chem.* **2012**, *84*, 1178−83.

(64) Gong, X.; Hu, Q.; Paau, M. C.; Zhang, Y.; Shuang, S.; Dong, C.; Choi, M. M. Red-Green-Blue Fluorescent Hollow Carbon Nanoparticles Isolated from Chromatographic Fractions for Cellular Imaging. *Nanoscale* **2014**, *6*, 8162−70.

(65) So, R. C.; Sanggo, J. E.; Jin, L.; Diaz, J. M. A.; Guerrero, R. A.; He, J. Gram-Scale Synthesis and Kinetic Study of Bright Carbon Dots from Citric Acid and Citrus Japonica *via* a Microwave-Assisted Method. *ACS Omega* **2017**, *2*, 5196−5208.

(66) Mitchell, H. D.; Markillie, L. M.; Chrisler, W. B.; Gaffrey, M. J.; Hu, D.; Szymanski, C. J.; Xie, Y.; Melby, E. S.; Dohnalkova, A.; Taylor, R. C.; Grate, E. K.; Cooley, S. K.; McDermott, J. E.; Heredia-Langner, A.; Orr, G. Cells Respond to Distinct Nanoparticle Properties with Multiple Strategies As Revealed by Single-Cell RNA-Seq. *ACS Nano* **2016**, *10*, 10173−10185.

(67) Klein, T.; Proppert, S.; Sauer, M. Eight Years of Single-Molecule Localization Microscopy. *Histochem. Cell Biol.* **2014**, *141*, 561−75.

(68) Thompson, R. E.; Larson, D. R.; Webb, W. W. Precise Nanometer Localization Analysis for Individual Fluorescent Probes. *Biophys. J.* **2002**, *82*, 2775−83.

(69) Shen, J.; Zhang, J. H.; Xiao, H.; Wu, J. M.; He, K. M.; Lv, Z. Z.; Li, Z. J.; Xu, M.; Zhang, Y. Y. Mitochondria Are Transported Along Microtubules in Membrane Nanotubes to Rescue Distressed Cardiomyocytes from Apoptosis. *Cell Death Dis.* **2018**, *9*, 81.

(70) Saxton, W. M.; Hollenbeck, P. J. The Axonal Transport of Mitochondria. *J. Cell Sci.* **2012**, *125*, 2095−104.

(71) Bian, J.; Li, J.; Kalytchuk, S.; Wang, Y.; Li, Q.; Lau, T. C.; Niehaus, T. A.; Rogach, A. L.; Zhang, R. Q. Efficient Emission Facilitated by Multiple Energy Level Transitions in Uniform Graphitic Carbon Nitride Films Deposited by Thermal Vapor Condensation. *ChemPhysChem* **2015**, *16*, 954−9.

(72) Miao, X.; Qu, D.; Yang, D.; Nie, B.; Zhao, Y.; Fan, H.; Sun, Z. Synthesis of Carbon Dots with Multiple Color Emission by Controlled Graphitization and Surface Functionalization. *Adv. Mater.* **2018**, *30*, 1704740.

(73) Zhang, Y.; Wang, Y.; Guan, Y.; Feng, L. Uncovering the Pka Dependent Fluorescence Quenching of Carbon Dots Induced by Chlorophenols. *Nanoscale* **2015**, *7*, 6348−55.

(74) Permatasari, F. A.; Aimon, A. H.; Iskandar, F.; Ogi, T.; Okuyama, K. Role of C−N Configurations in the Photoluminescence of Graphene Quantum Dots Synthesized by a Hydrothermal Route. *Sci. Rep.* **2016**, *6*, 21042.

(75) Yuan, F.; Wang, Z.; Li, X.; Li, Y.; Tan, Z.; Fan, L.; Yang, S. Bright Multicolor Bandgap Fluorescent Carbon Quantum Dots for Electroluminescent Light-Emitting Diodes. *Adv. Mater.* **2017**, *29*, 1604436.

(76) Zhan, J.; Geng, B. J.; Wu, K.; Xu, G.; Wang, L.; Guo, R. Y.; Lei, B.; Zheng, F. F.; Pan, D. Y.; Wu, M. H. A Solvent-Engineered Molecule Fusion Strategy for Rational Synthesis of Carbon Quantum Dots with Multicolor Bandgap Fluorescence. *Carbon* **2018**, *130*, 153−163.

(77) Lakowicz, J. R. *Principles of Fluorescence Spectroscopy*; Springer Science & Business Media: Berlin, 2013.

(78) Valeur, B.; Berberan-Santos, M. N. *Molecular Fluorescence: Principles and Applications*; John Wiley & Sons: New York, 2012.

(79) Berezin, M. Y.; Achilefu, S. Fluorescence Lifetime Measurements and Biological Imaging. *Chem. Rev.* **2010**, *110*, 2641−84.

(80) Gan, Z.; Xu, H.; Hao, Y. Mechanism for Excitation-Dependent Photoluminescence from Graphene Quantum Dots and Other Graphene Oxide Derivates: Consensus, Debates and Challenges. *Nanoscale* **2016**, *8*, 7794−807.

(81) Hu, D.; Zhao, B.; Xie, Y.; Orr, G.; Li, A. D. Understanding Super-Resolution Nanoscopy and Its Biological Applications in Cell Imaging. *Phys. Chem. Chem. Phys.* **2013**, *15*, 14856−61.

(82) Cui, Y.; Hu, D.; Markillie, L. M.; Chrisler, W. B.; Gaffrey, M. J.; Ansong, C.; Sussel, L.; Orr, G. Fluctuation Localization Imaging-Based Fluorescence *in situ* Hybridization (Flifish) for Accurate Detection and Counting of RNA Copies in Single Cells. *Nucleic Acids Res.* **2018**, *46*, e7.